

Chapter 17

Radar Interferometers

The next set of radar applications we are going to introduce is interferometric radar. For the environmental applications we have been emphasizing here, interferometric analyses have found their most widespread use in imaging radars. And because imaging radars generally require fine resolution and synthetic aperture processing, the systems we are most interested are interferometric synthetic aperture radars. Thus you will often see the nomenclature InSAR as an acronym (ISAR was already in common usage as an abbreviation for inverse synthetic aperture radar.)

We will see that a geometric interpretation of radar phase is a very useful way to visualize and model interferometric echoes. While the development of classical interferometers at light or radio wavelengths precedes InSAR by several or more decades, much of this work was aimed at making interferometry work using technologies that did not permit ready measurement of signal phase. In today's digital world we can sample and record complex signals easily, bypassing the need for intermediate conversion to power quantities that characterizes classical interferometry. Nonetheless it is worthwhile to briefly examine classical development for its precursory role in radar interferometry.

An interferometer is a device that analyzes EM waves coherently at two observation points, that is, the phase difference of two waves is studied. Combining the signals from both antennas to determine the phase difference forms the interferometer. As it was difficult to measure the two signal phases in the pre-digital era, there evolved two main implementations that exploited amplitude quantities dependent on phase- adding interferometers and multiplying or correlation interferometers. Both have been used at radar wavelengths, although

the latter is more common today. Because the adding interferometer was developed first, and is perhaps conceptually simpler, it is worthwhile to take a look at the basic principles of interferometry from this viewpoint.

17.1 Adding interferometer

We have seen that we can measure the amplitude and frequency for an arriving EM wave, which in the case of a radar is an echo reflected from an object of interest. It also important in many applications to know the direction of arrival as well, such as in mapping the location of a radioastronomical source or of an incoming nuclear missile. Examine the geometry of a wave field on a pair on antennas as shown in fig. 17.1. The wave travels a distance $\delta = B \cdot u_{inc} = B \sin \alpha$ longer to reach the second antenna, accumulating additional phase in the amount $\frac{2\pi}{\lambda} \delta$. Note that the projection of B in the incident direction is written using a $\sin()$ rather than $\cos()$ because we have defined the angle of arrival α in the off-zenith direction rather than with respect to the horizon. The factor of 2 becomes a factor of 4 if we have two independent radar systems, one at the location of antenna 1 and one at the location of antenna 2, as the extra path length is traversed twice. For a cosinusoidal incoming wave, we will find it convenient to consider the signal from the first antenna as advanced by half of this phase and the signal from the second antenna as delayed by half of this amount:

$$s_1(t) = a \exp[-j(2\pi ft + \frac{2\pi}{\lambda} \frac{\delta}{2})] \quad (17.1)$$

and

$$s_2(t) = a \exp[-j(2\pi ft - \frac{2\pi}{\lambda} \frac{\delta}{2})] \quad (17.2)$$

where a is the amplitude of the incoming wave. The adding interferometer obtains its output signal by summing the two waves coherently,

$$\begin{aligned} c_{sum}(t) &= s_1(t) + s_2(t) \\ &= a \exp[-j(2\pi ft + \frac{2\pi}{\lambda} \frac{\delta}{2})] + a \exp[-j(2\pi ft - \frac{2\pi}{\lambda} \frac{\delta}{2})] \\ &= a \exp[-j(2\pi ft)] 2 \cos(\frac{2\pi}{\lambda} \frac{\delta}{2}) \\ &= a \exp[-j(2\pi ft)] 2 \cos(\frac{2\pi}{\lambda} \frac{B \sin \alpha}{2}) \end{aligned} \quad (17.3)$$

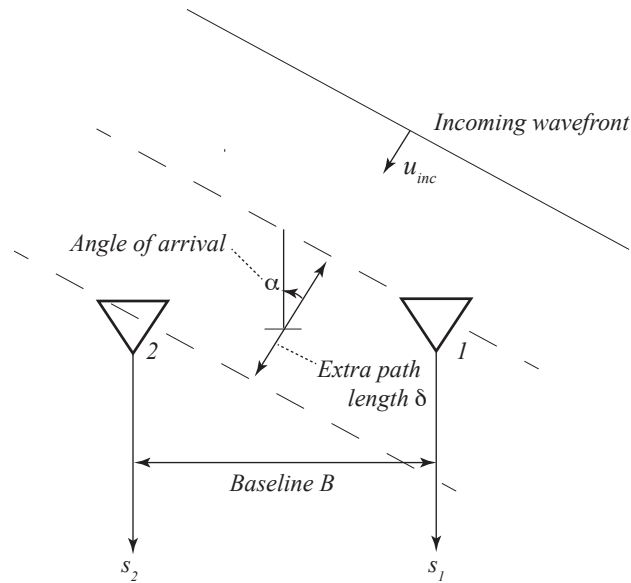


Figure 17.1: Wavefront on two antennas. A plane wave in the direction of unit vector u_{inc} impinges on two antennas separated by a baseline B . The extra path length traveled by the wave from the first antenna encountered δ is equal to $B \cdot u_{inc} = B \sin \alpha$, and accumulates extra phase in the amount $\frac{2\pi}{\lambda} \delta$. If each antenna both transmits and receives, then the path difference is traversed twice, and the phase shift is $\frac{4\pi}{\lambda} \delta$. An interferometer sensitive to the phase difference can thus determine the location of the source.

The received signal amplitude is multiplied by a cosine factor that depends on angle of arrival, so that measuring the power of the signal tells us something about its location. In fact, eq. 17.3 shows that the amplitude of the sum signal is proportional to the component of the source distribution with a spatial frequency determined by the baseline length and the angle of arrival.

17.2 Monopulse radar

The adding interferometer converts phase information to amplitude. This is especially valuable for radioastronomical instruments where sensitivity to a single or set of Fourier coefficients of the sky distribution is desired. For a radar system, where there may be only a single point target of interest, however, this observation of signal power depends not only on arrival angle but also on intrinsic brightness (denoted a above) of the object, which is usually unknown. A variation of the adding interferometer, denoted monopulse because it can be implemented on a single radar echo, removes the dependence on knowledge of signal amplitude by considering the ratio of two quantities, so that the absolute amplitude of the echo cancels out.

When we formed the adding interferometer signal (eq. 17.3), we computed the sum of the signals from the two antennas. For monopulse, we also form the difference of the two signals, as

$$\begin{aligned}
 c_{diff}(t) &= s_1(t) - s_2(t) \\
 &= a \exp[-j(2\pi ft + \frac{2\pi \delta}{\lambda} \frac{\delta}{2})] - a \exp[-j(2\pi ft - \frac{2\pi \delta}{\lambda} \frac{\delta}{2})] \\
 &= a \exp[-j(2\pi ft)] 2j \sin(\frac{2\pi \delta}{\lambda} \frac{\delta}{2}) \\
 &= a \exp[-j(2\pi ft)] 2j \sin(\frac{2\pi B \sin \alpha}{\lambda} \frac{\delta}{2})
 \end{aligned} \tag{17.4}$$

Now we can form the ratio of the magnitude of each of the difference and sum measurements, and obtain

$$\frac{\sin(\frac{2\pi B \sin \alpha}{\lambda} \frac{\delta}{2})}{\cos(\frac{2\pi B \sin \alpha}{\lambda} \frac{\delta}{2})} = \tan \frac{2\pi B \sin \alpha}{\lambda} \frac{\delta}{2} \tag{17.5}$$

Thus the amplitude a of the incoming wave cancels out, so that the ratio of the difference and sum amplitudes depends solely on the angle of arrival. Such a differential measurement permits a much less ambiguous determination of angle of arrival.

17.3 A simple multiplying interferometer

Accurate measurement of the phase of an incoming wave on two antennas allows us to determine the angle of arrival. With today's technology we can measure this phase directly, without requiring the intermediate step of conversion to magnitude, and derive the angle of arrival more accurately.

Let's examine a radar interferometer design for measuring surface topography. We will see that this is equivalent to measuring the angle of arrival from a point of interest on the surface, as long as we know the platform altitude and the baseline between the two radar antennas. Consider a radar geometry similar to the adding interferometer figure but altered so as to put the antennas on an observing platform looking down at the surface, as in fig. 17.2. Similar to the adding interferometer, the extra path length to the second antenna is the projection of the baseline in the radar line of sight:

$$\delta = B \sin(\theta - \alpha) \tag{17.6}$$

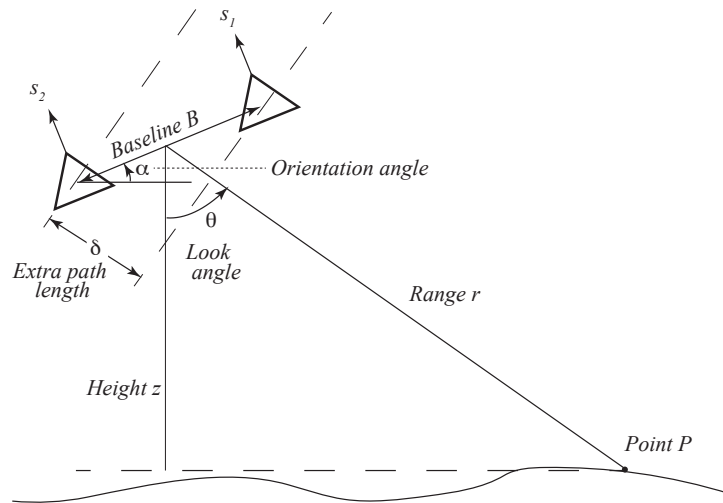


Figure 17.2: Radar interferometer geometry. Two radar antennas on an airborne or spaceborne platform illuminate a point on the surface below. The range from the antenna array center to the point is r , and the range difference from the first to the second antenna is δ , where δ as before is the projection of the baseline B in the line of sight from the radar to the point P .

For this and the examples in the rest of this chapter, let us assume a system configuration where we treat each antenna as a complete radar system, that is, we transmit and receive signals from both positions and record the echo from each at each. This will usually be the appropriate model for spaceborne platforms, where synchronization of multiple satellites is challenging, though not impossible. For our purposes, the only difference between this approach and one in which we transmit at a single position and receive at two locations is the change from a factor of 2 to a factor of 4 in the phase accumulated for each wavelength of extra path length δ . Under the two transmitter assumption the factor is 4, hence the measured signals at antennas 1 and 2 respectively are then

$$s_1(t) = a \exp\left[-j \frac{4\pi}{\lambda} \left(r(t) - \frac{\delta(t)}{2}\right)\right] \quad (17.7)$$

and

$$s_2(t) = a \exp\left[-j \frac{4\pi}{\lambda} \left(r(t) + \frac{\delta(t)}{2}\right)\right] \quad (17.8)$$

where both r and δ vary with echo time as we are imaging a surface. Instead of adding these two signals, we form the product of s_1 with the conjugate of s_2 , to form the interferometric

image i :

$$\begin{aligned}
 i(t) &= s_1(t) \cdot s_2(t)^* \\
 &= a \exp[-j \frac{4\pi}{\lambda} (r(t) - \frac{\delta(t)}{2})] \cdot a \exp[+j \frac{4\pi}{\lambda} (r(t) + \frac{\delta(t)}{2})] \\
 &= a^2 \exp[j \frac{4\pi}{\lambda} B \cos(\theta(t) - \alpha)]
 \end{aligned} \tag{17.9}$$

The measured interferogram phase $\phi(t)$ for a point on the surface then yields θ for that point, if the other parameters are known:

$$\phi(t) = \arg [i(t)] \tag{17.10}$$

$$\theta(t) = \arcsin[\frac{\lambda\phi(t)}{4\pi B}] + \alpha \tag{17.11}$$

Recall that our goal here is to measure the topography at point P . Completing the triangle shown in fig.17.2, we see that we can obtain the height from P to the altitude z of the platform as

$$z = r \cos \theta(t) \tag{17.12}$$

In other words, the InSAR phase at each point on the surface can be interpreted as the elevation of that point, or more precisely, the distance below the platform of every point.

A more subtle point here is that we have assumed that the two echoes received at a time t correspond to exactly the same point on the ground, which will not be true if the ranges from the point to the two antennas differ. The signals must be aligned in time for the phase to have the relation of eq. 17.9, so that rather than a simple multiplication, we compute the correlation of the two signals and select the phase at the correlation peak. Hence we are in fact implementing a *correlation interferometer* instead of the multiplying interferometer. Once the signals are properly aligned so that echoes from each point on the surface match in both channels, the multiplying equation results hold.

17.4 Geometrical interpretation of phase difference

The discussion of the the multiplying interferometer in section 17.3 uses a simplification in which we modeled the incoming wavefront as a plane wave, an approximation that holds for a target at infinite distance. We can be more accurate and accommodate objects at any distance

if we use a more general geometry and interpret the measurements geometrically as path length differences rather than as angle of arrival. The more general configuration is shown in fig. 17.3. We note that we quantify the distances to the two antennas as r_1 and r_2 , without requiring plane wave incidence, so that the signals we receive and measure as interferometric phase may be given in terms of the difference $r_1 - r_2$:

$$\begin{aligned} s_1(t) &= e^{-j(\frac{4\pi}{\lambda}r_1 - \omega t)} \\ s_2(t) &= e^{-j(\frac{4\pi}{\lambda}r_2 - \omega t)} \\ s_1(t)s_2^*(t) &= e^{-j\frac{4\pi}{\lambda}(r_1 - r_2)} \end{aligned}$$

so the interferometer phase $\phi = \frac{4\pi}{\lambda}(r_1 - r_2)$. Note that we have omitted the signal amplitude a in these equations as we have already established that it does not affect the phase retrieval.

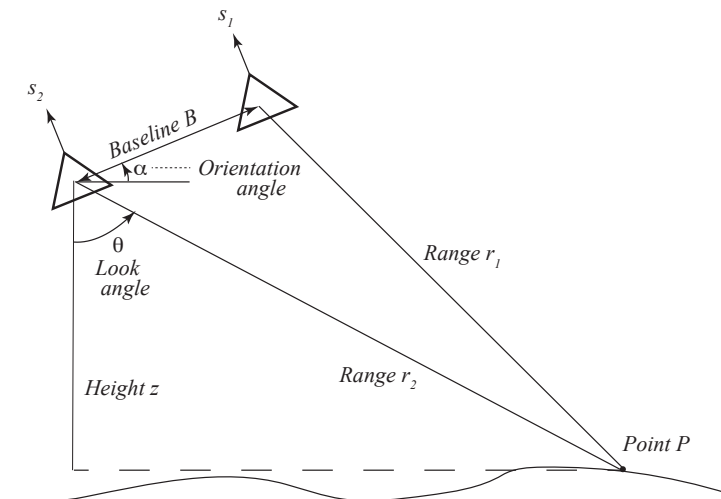


Figure 17.3: Path length differences. The distances from the point of interest to the two antennas are r_1 and r_2 , and the InSAR phase is the difference of the ranges multiplied by $\frac{4\pi}{\lambda}$.

17.5 Measuring topography without the parallel ray approximation

Accurate determination of topographic elevation requires solving for the two triangles illustrated in fig. 17.3. Consider first the triangle formed by the two antennas and the point to be imaged P . We relate the ranges r_1 and r_2 to the baseline length $|B|$ using the law of cosines:

$$\begin{aligned} r_1^2 &= r_2^2 + |B|^2 - 2r_2|B| \cos\left(\frac{\pi}{2} - \theta + \alpha\right) \\ &= r_2^2 + |B|^2 - 2r_2|B| \sin(\theta - \alpha) \end{aligned}$$

Rearranging to find the enclosed angle,

$$2r_2|B| \sin(\theta - \alpha) = r_2^2 - r_1^2 + |B|^2 \quad (17.13)$$

$$\begin{aligned} |B| \sin(\theta - \alpha) &= \frac{r_2^2 - r_1^2 + |B|^2}{2r_2} \\ &= \frac{(r_2 + r_1)(r_2 - r_1) + |B|^2}{2r_2} \\ &\doteq \frac{2r_2(r_2 - r_1) + |B|^2}{2r_2} \\ &= \frac{\delta 2r_2 + |B|^2}{2r_2} \\ &= \frac{\phi\lambda}{4\pi} + \frac{|B|^2}{2r_2} \end{aligned} \quad (17.14)$$

Once we have calculated $\sin(\theta - \alpha)$, we use that quantity to solve for the height z as before. It is also worth noting that eq. 17.14 reduces to our previous result (eq. 17.11) when $r_2 \gg |B|$.

17.6 Measurement accuracy

We have seen that we can relate the phase observed in a radar interferometer to the topographic elevation of a surface. Let us now see how accurately we can make that determination, and what factors in a radar system contribute most significantly to the error in measurement. Note that we can make several kinds of errors, two of which are i) phase errors (ϕ) and ii) tilt errors (α). The effect of each error class is different: phase errors are uncorrelated from point to point, while tilt errors tilt the entire output image.

We can quantify the uncertainty of our height (z) determination by computing the partial derivatives of the height with respect to our system parameters.

Measuring phase. The interferometer resolves height through measurement of the phases of radar echoes. We need to be able to relate the accuracy of these phases to system parameters, such as SNR. To quantify this, refer to fig. 17.4. The phase we observe ϕ is the angle of the

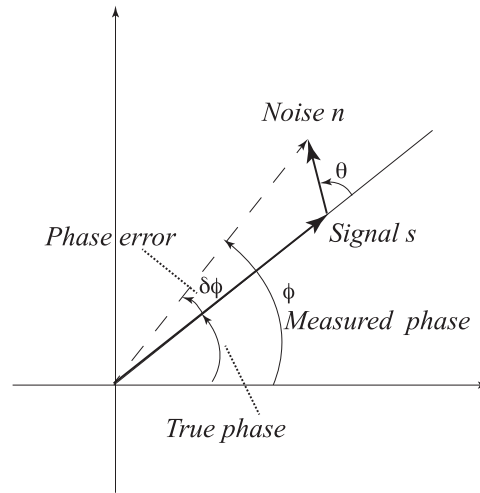


Figure 17.4: Phase noise. We measure a phase ϕ that is the angle of the sum of a complex (vector) signal plus a noise term. The higher the signal to noise ratio, that is the ratio of the vector lengths, the smaller the phase error will be.

vector sum of the signal and a noise term. The ratio of the lengths of the signal and noise is the square root of the signal to noise ratio, because the lengths of the vectors are amplitude and not power quantities:

$$\frac{|s|}{|n|} = \sqrt{(SNR)} \quad (17.15)$$

The measured phase error $\delta\phi$ will be

$$\begin{aligned} \delta\phi &= \arctan \frac{|n| \sin \theta}{|s| + |n| \cos \theta} \\ &= \arctan \frac{\sin \theta}{\sqrt{(SNR)} + \cos \theta} \end{aligned}$$

The noise term $|n|$ and its direction θ will not be constant for every measurement, thus the phase error $\delta\phi$ can only be described by its statistics. In a model where the noise is assumed

to be drawn from a bivariate Gaussian distribution, we can model the pdfs of the angle as a uniform random variable and of the amplitude as a Rayleigh random variable. For unit variance of the bivariate Gaussian in both axes, we obtain

$$p_\theta(\theta) = \frac{1}{2\pi}, \quad \theta = [0, 2\pi) \quad (17.16)$$

and

$$p_{|n|}(|n|) = 2|n| \exp(-|n|^2), \quad |n| = [0, \infty) \quad (17.17)$$

Then the first and second moments of $\delta\phi$ would be

$$\mu_1 = \int_0^\infty \int_0^{2\pi} \arctan \frac{|n| \sin \theta}{\sqrt{(SNR)} + |n| \cos \theta} p_\theta(\theta) p_{|n|}(|n|) d\theta d|n| \quad (17.18)$$

and

$$\mu_2 = \int_0^\infty \int_0^{2\pi} \left(\arctan \frac{|n| \sin \theta}{\sqrt{(SNR)} + |n| \cos \theta} \right)^2 p_\theta(\theta) p_{|n|}(|n|) d\theta d|n| \quad (17.19)$$

from which we can calculate the standard deviation σ_ϕ . These integrals are complicated to derive analytically, but can be readily computed numerically. Fig. 17.5 shows numerical evaluations (black dots) for several values of SNR, along with a good approximation that is often used for InSAR phase noise:

$$\sigma_\phi = \frac{\sqrt{1 + 2SNR}}{SNR} \frac{1}{2\sqrt{N}} \quad (17.20)$$

where N is the number of complex pixels averaged, or ‘looks.’ Increasing the number of looks has a similar effect as increasing SNR as both represent a coherent sum that adds signal in phase and noise by power only.

Phase errors. Now let us return to the accuracy of our elevation estimates. We derived a relation between the height z of a surface and InSAR phase in two coupled equations, which we repeat:

$$|B| \sin(\theta - \alpha) = \frac{\phi\lambda}{4\pi} + \frac{|B|^2}{2r_2} \quad (17.21)$$

and then solve for height:

$$z = r \cos \theta \quad (17.22)$$

Our needed sensitivity is how z varies with ϕ , or the derivative $\frac{\partial z}{\partial \phi}$. But our two equations do not yield this result straight-forwardly, so instead we compute intermediate derivatives $\frac{\partial \theta}{\partial \phi}$ and

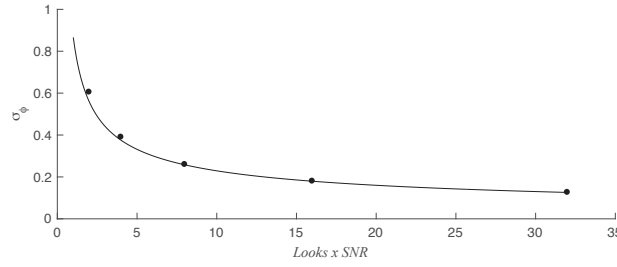


Figure 17.5: Phase noise as a function of SNR. InSAR phase noise decreases as the SNR increases. Black dots show numerical evaluation of eq. 17.19, and the solid line shows the useful approximation eq. 17.20. The approximate expression includes the number of looks (here 1), as averaging over pixels to form looks leads to the signal adding coherently with the noise adding incoherently. Thus increasing looks has a similar effect as increasing SNR. Both improve the accuracy as the square root of the increase.

$\frac{\partial z}{\partial \theta}$, whose product is the needed relation. So our approach is to calculate first

$$\begin{aligned} \frac{\partial}{\partial \theta} |B| \sin(\theta - \alpha) &= \frac{\partial}{\partial \phi} \left[\frac{\phi \lambda}{4\pi} + \frac{|B|^2}{2r_2} \right] \\ |B| \cos(\theta - \alpha) \partial \theta &= \frac{\lambda}{4\pi} \partial \phi \end{aligned}$$

and then infer

$$\frac{\partial \theta}{\partial \phi} = \frac{\lambda}{4\pi} \frac{1}{|B| \cos(\theta - \alpha)} \quad (17.23)$$

Noting that uncertainties in α and θ are equivalent save for change in sign, repeating a simpler argument for $\frac{\partial z}{\partial \theta}$,

$$\frac{\partial z}{\partial \theta} = r \sin \theta$$

Now we compute the product to get the desired derivative:

$$\frac{\partial z}{\partial \phi} = \frac{\partial z}{\partial \theta} \frac{\partial \theta}{\partial \phi} = \frac{\lambda}{4\pi} \frac{r \sin \theta}{|B| \cos(\theta - \alpha)} \quad (17.24)$$

Stating this in terms of the uncertainties in z and ϕ , σ_z and σ_ϕ , respectively,

$$\sigma_z = \frac{\lambda}{4\pi} \frac{r \sin \theta}{|B| \cos(\theta - \alpha)} \sigma_\phi \quad (17.25)$$

We can get a feel for how accurate this might be in practice by looking at some nominal

system parameters. Suppose we can measure ϕ to an accuracy of about 0.1 rad, or about 6° . In an aircraft system, assuming an orientation angle $\alpha=0$, with $r = 10$ km, a wavelength of 0.06 m, look angle 30° , and baseline distance 1 m, our height accuracy would be

$$\begin{aligned}\sigma_z &= \frac{0.06}{4\pi} \frac{10000 \cdot 0.5}{1 \cdot 0.866} \cdot 0.1 \\ &= 2.8\text{m}\end{aligned}$$

So with such an aircraft system the contribution to measurement error from phase noise is 2.8 m. A similar set of computations for the error due to tilt, and noting that uncertainty in α has the same effect but with negative sign as uncertainty in θ , follows from the derivative of z with respect to θ we calculated above. In terms of uncertainties then,

$$\sigma_z = r \sin \theta \sigma_\theta$$

which for the aircraft system example here, and assuming we can measure the tilt to 0.001 rad,

$$\begin{aligned}\sigma_z &= 10000 \cdot 0.5 \cdot 0.001 \\ &= 5\text{m}\end{aligned}$$

Thus you can see that for this system, if the uncertainties in the system are as used here, the overall accuracy will be dominated by tilt rather than phase noise errors.

In a spaceborne implementation, we will very often use two separate satellites, or a single satellite in a nearly repeating orbit, to form the interferometer baseline. The use of multiple platforms allows us to choose the baseline length, since we are not restricted to a single structure supporting two antennas, which is constrained by the size of the orbiting platform. Why is this helpful? Suppose we can measure the relative orbit position accuracy across-track to 10 cm, which is easily achievable for many orbital systems today. Then the accuracy of the virtual tilt angle α is $10 \text{ cm}/|B|$ rad. For 100 m satellite separation, $\sigma_\alpha = 0.1/100 = 10^{-3}$, while for a 1 km baseline $\sigma_\alpha = 10^{-4}$.

For this configuration, both the uncertainty due to phase noise (eq.17.25) and tilt decrease with baseline length. So it might seem that the best accuracy would result from allowing the baseline length to grow as large as possible. For an aircraft system there is a limit to the baseline

length set by the dimensions of the aircraft itself, but for two satellites very large separations are possible. But, as we are about to see, longer baselines lead to more noise in the phase measurement, and hence an engineering tradeoff exists in the baseline length design.

17.7 Decorrelation

We see that the error in our measurement is minimized for as $|B|$ becomes larger and larger, so it might seem that we should always seek to maximize $|B|$. But there is another effect that increases phase noise if we let $|B|$ grow without limit. This additional noise source is called baseline decorrelation noise, and it arises because we have viewed the surface from two view points that are dissimilar.

Physically what is happening is at each resolution element we measure the coherent sum of reflected waves from each individual scattering center in that element. If we change the viewing geometry, the waves will add in a different fashion and the average phase will not be preserved (fig. 17.6). We want to determine the degree to which the phases from the sums of all the

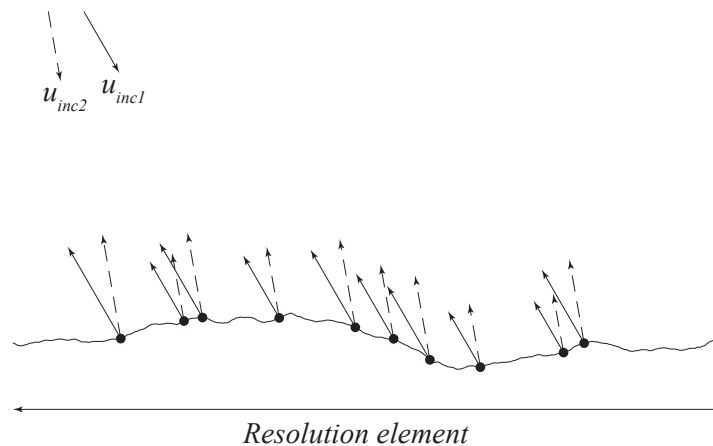


Figure 17.6: Spatial decorrelation noise. For each resolution element, we observe the coherent sum of the reflected waves from each scattering center in the element. If we change the incidence angle, here from u_{inc1} to u_{inc2} , the waves will add to a different value as their line of sight paths differ. The mean phase of the total return wave (ϕ) will vary as the wave directions change.

points ϕ are related to each other, or, more formally, correlated.

For this calculation we consider the radar return from a resolution element defined using

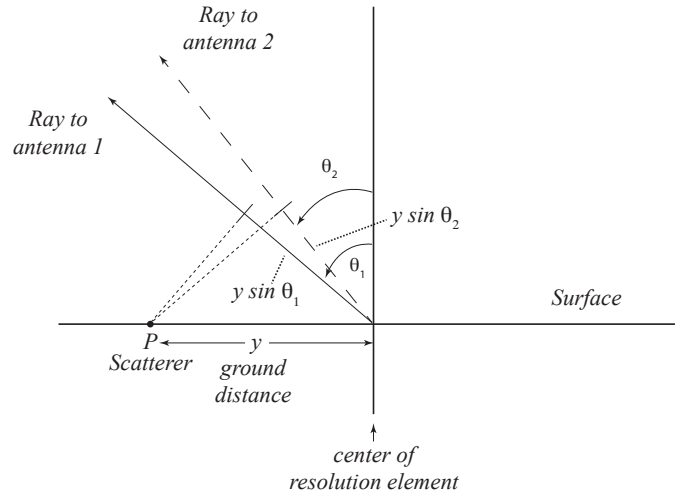


Figure 17.7: Spatial decorrelation geometry. Quantities needed to calculate the correlation between two radar echoes as we vary the separation of the incidence angles for each signal. The phase of a reflected wave from a single scatterer P changes as the line of sight distance $y \sin \theta$ from the center of the resolution element changes.

ground range coordinates where the along-track (azimuth) coordinate is x , and the across-track y . Referring to fig. 17.7, the left-right dimension represents a slice in the y direction, with the x direction into the page. We model the total signal s_1 measured at antenna 1, at incidence angle θ_1 corresponding to u_{inc1} , as the sum of returns from all points on the surface:

$$s_1 = \iint f(x - x_0, y - y_0) \exp \left[-j \frac{4\pi}{\lambda} (r + y \sin \theta_1) \right] w(x, y) dx dy \quad (17.26)$$

where r is the range to the center of the resolution element (x_0, y_0) , $w(x, y)$ is the impulse response of the system, and $f(x - x_0, y - y_0)$ is the complex reflectivity of surface position.

Similarly, for s_2 :

$$s_2 = \iint f(x - x_0, y - y_0) \exp \left[-j \frac{4\pi}{\lambda} (r + y \sin \theta_2) \right] w(x, y) dx dy \quad (17.27)$$

The complex product $s_1 s_2^*$ is thus the following complicated-looking integral:

$$s_1 s_2^* = \iiint \iint f(x - x_0, y - y_0) f^*(x' - x_0, y' - y_0) \cdot \exp \left[-j \frac{4\pi}{\lambda} y (\sin \theta_1 - \sin \theta_2) \right] w(x, y) w^*(x', y') dx dy dx' dy' \quad (17.28)$$

We can greatly simplify this expression if we assume that the scattering at each point on the surface is uncorrelated from every other point, so that the autocorrelation function of the surface reflectivity is a δ -function:

$$\langle f(x, y) f^*(x', y') \rangle = \sigma^0 \delta(x - x', y - y') \quad (17.29)$$

reducing the integral to

$$\langle s_1 s_2^* \rangle = \sigma^0 \iint \exp[-j \frac{4\pi}{\lambda} y \cos \theta \delta \theta] |w(x, y)|^2 dx dy \quad (17.30)$$

where $\theta = (\theta_1 + \theta_2)/2$ and $\delta \theta = \theta_1 - \theta_2$. Normalizing the average $\langle s_1 s_2^* \rangle$ to unity at zero separation defines the *spatial correlation* of the interferogram, which tells us how well related two echoes are as we vary the separation of the look angles. We define the correlation of the two signals as the magnitude of the normalized cross product $|\langle s_1 s_2^* \rangle|$. We recognize eq.

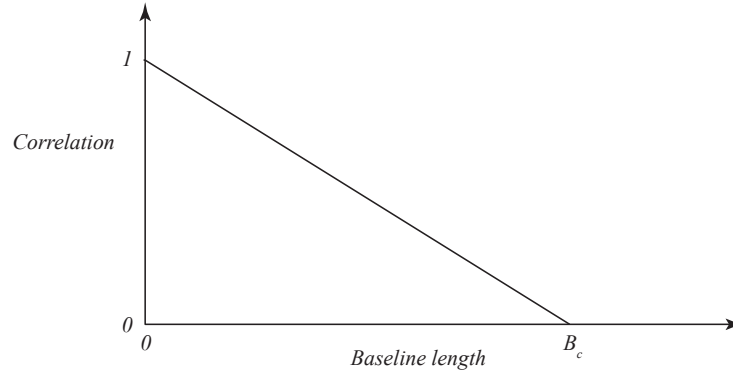


Figure 17.8: Correlation from idealized impulse response. If the radar impulse is well-characterized by a $\text{sinc}()$ function, the degree of correlation as we increase the baseline length falls off as a triangle function, reaching zero at a maximum baseline length B_c , denoted the *critical baseline*.

17.30 as the Fourier transform with respect to $\delta \theta$ of the square of the impulse response. If the impulse response is $\text{sinc}(x) = \frac{\sin \pi x}{\pi x}$, then the transform of its square is a triangle function, which normalized to express correlation yields,

$$\rho_{\text{spatial}} = 1 - \frac{2 \cos \theta \delta_y d \theta}{\lambda} \quad (17.31)$$

δ_y being range resolution projected onto the ground. Changing the dependence on angle to

Aircraft C – band system :	$\sim 100m$
Satellite L – band system :	$\sim 5000m$
Satellite C – band system :	$\sim 1250m$

Table 17.1: Typical InSAR critical baselines.

dependence on baseline length, we can define B_{\perp} as the component of the baseline perpendicular to the line of sight, and thus the difference angle

$$d\theta = \frac{B_{\perp}}{r} \quad (17.32)$$

Combining this with eq. 17.31 we obtain a similar triangle function that goes to zero when the baseline reaches a critical value $B_c = \frac{\lambda r}{2 \cos \theta \delta_y}$. The critical baseline represents the maximum distance allowed between antennas if the interferogram phase is to be of nonzero average. In a practical system, we must limit the baseline to a value somewhat smaller than the critical value to keep the correlation at an acceptable level. Thus again we have a trade off to make: the baseline needs to be long enough to be sensitive to topographic variation but not so long as to be poorly correlated.

It is useful to keep a few typical values in as a starting point for the design of an InSAR system. Table 17.1 lists several values of B_c for airborne and spaceborne platforms at common wavelengths and moderate (~ 5 - 10 m) resolution. Keeping the noise from decorrelation at an acceptable level, we would prefer to operate at about 10 - 20% of B_c . But that value tends to be too long to implement on an aircraft or a single satellite. Thus, for aircraft we usually have a relatively short baseline and make up for the ϕ -sensitivity with high SNR, while for spacecraft we often prefer a single satellite in a repeat-pass mode, our next topic.

17.8 Decorrelation and SNR

It may seem that decorrelation and signal to noise ratio are related, and in fact they are different ways of describing the same statistics of radar measurements. We can readily derive one from the other¹.

Let's begin by defining two different measurements of a repeating signal plus a variable noise component, as we illustrated above in fig. 17.4. Denote these two measurements as

$$\begin{aligned} m_1 &= s + n_1 \\ m_2 &= s + n_2 \end{aligned}$$

where s is the common signal vector and n_1, n_2 are the noise components of each. As before, the ratio of signal power to noise power is the SNR:

$$\text{SNR} = \frac{|s|^2}{|n_i|^2} \quad (17.33)$$

We calculate the correlation ρ of the two measurements through the usual definition:

$$\begin{aligned} \rho &= \frac{\langle m_1 m_2^* \rangle}{\sqrt{\langle m_1 m_1^* \rangle} \sqrt{\langle m_2 m_2^* \rangle}} \\ &= \frac{\langle (s + n_1) (s + n_2)^* \rangle}{\sqrt{\langle (s + n_1) (s + n_1)^* \rangle} \sqrt{\langle (s + n_2) (s + n_2)^* \rangle}} \end{aligned}$$

We can assume that the signal and noise components are independent and thus uncorrelated, as are the two noise instances. The expectations in eq. 17.34 then reduce to

$$\begin{aligned} \rho &= \frac{|s|^2}{|s|^2 + |n|^2} \\ &= \frac{1}{1 + \text{SNR}^{-1}} \end{aligned}$$

As we might expect, if the SNR grows very large, ρ approaches unity. And if the SNR goes to zero, so does the correlation. We can use either SNR or ρ to describe the statistics of our phase measurements. Sometimes it will be more useful to employ the SNR measure, and sometimes the decorrelation will prove more valuable.

¹We often mix the terms correlation and decorrelation, which is fine as long as we remember that correlation (ρ) = 1 - decorrelation.

17.9 Repeat-track Orbital Interferometry

We have just seen that we would like to use baselines of several hundred meters in length for spaceborne interferometric observations, and such distances are too large for single spacecraft construction. The way around this is either to use two spacecraft flying in formation (often very expensive!) or to use one spacecraft flying in a repeat orbit.

Recall that we have modeled the return from a resolution element as the sum of echoes from a randomly distributed set of scatterers on the ground. What happens if we view the same region again at a later time? If none of the scatterers has moved, the return will be exactly the same except for the system noise component. Thus repeat-orbit geometries can form interferometers over unchanging terrain.

What if the scatterers have indeed moved around? If the motions are random and on the order of a wavelength or more in size, the sum of the echoes will have a different propagational phase and there will no longer be correlation between the two radar echoes. It will be the same as if we had imaged the area with a spatial baseline exceeding the critical value.

But if the random motion is much smaller, we have a tool for characterizing surface changes at the wavelength scale. Using an argument following eqs. 17.26 - 17.30 and allowing the position of each scatterer to move according to a Gaussian-distributed distance in each dimension, we can show that the amount of decorrelation from surface movement is related to amount of motion and wavelength by

$$\rho_{\text{temporal}} = \exp\left[-\frac{1}{2}\left(\frac{4\pi}{\lambda}\right)^2[\sigma_y^2 \sin^2 \theta + \sigma_z^2 \cos^2 \theta]\right] \quad (17.34)$$

where we define ρ_{temporal} as the correlation for temporally-spaced observations, and σ_y and σ_z are the rms y and z motions. As was the case for spatial decorrelation, the temporal decorrelation will be at an acceptably low level as long as the motions are smaller than a large fraction of a wavelength.

As long as the temporal correlation is high, which means that the random motion of scatterers in each resolution element is small, we can proceed as we did in the fixed array case above and form interferograms from the spaceborne images. We need to preserve the phase of each image to be able to calculate the phase differences, so we will require complex valued images, as we needed for the multiplying interferometer described earlier.

An example of an elevation (topography) map derived from a set of repeat pass spaceborne

radar images is shown in fig. 17.9. These data were acquired over the island of Hawaii by the Sentinel-1A and -1B spacecraft between Nov. 2019 and March 2020. The complex interferogram resulting from the multiplying interferometer formed by two satellite passes yields the height, and in this figure several interferograms were averaged to reduce system noises. Elevation is shown as color, with contour lines added every 1000 m of altitude.

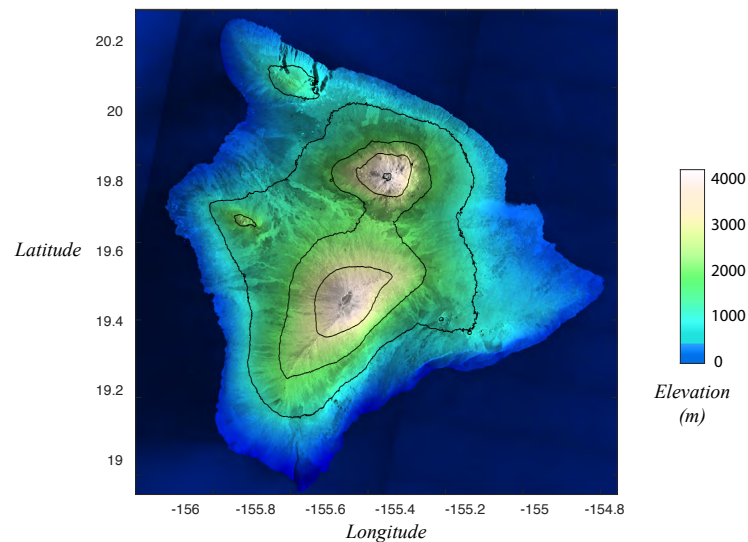


Figure 17.9: Elevation map of island Hawaii derived from repeat pass Sentinel-1A and -1B radar satellites. Estimates from several interferograms are averaged to reduce system noise. Brightness is radar backscatter magnitude, height coded as color. Contour lines depict heights at 1000, 2000, 3000, and 4000 m.

17.10 Motion Measurements

The main difference between the repeat orbit implementation and the fixed two-element array is that the two images are acquired at different times. This leads to sensitivity to mean motion of each resolution element, as the phase difference can change systematically, shifting the mean value of the phase difference but without appreciably affecting its variance.

To see this, suppose that instead of random motion, the surface scatterers move together toward or away from the radar. In this case, as a good approximation the phase of each scatterer's echo changes by the same amount. Thus there will be no decorrelation, but instead an average phase change will be observed in the interferogram.

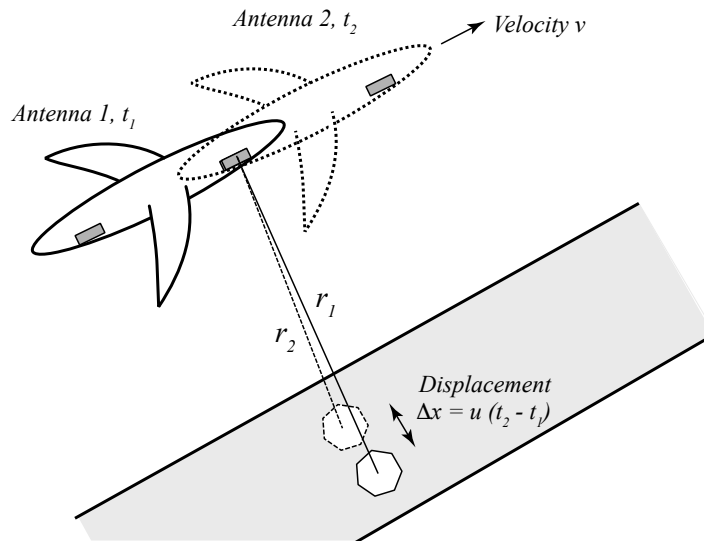


Figure 17.10: Ocean current geometry. An aircraft system for observing ocean currents in which a patch of ocean is first observed at time t_1 and range r_1 (solid line airframe) by an antenna mounted forward on the aircraft body, and at a second time t_2 with range r_2 (dotted line airframe) by an antenna mounted aft on the aircraft. If there is a current u on the surface, the range will change by $\Delta x \sin \theta = u \cdot (t_2 - t_1) \cdot \sin \theta$ in the time it takes the aircraft to fly the distance between its two antennas.

We can illustrate an InSAR system measuring the surface at two different times by an example of an aircraft measuring ocean currents (fig. 17.10). In this implementation, a patch of ocean is first observed at time t_1 and range r_1 (solid line airframe) by an antenna mounted forward on the aircraft body, and at a second time t_2 with range r_2 (dotted line airframe) by an antenna mounted aft on the aircraft. In the case when there is no motion of the surface, the two measurements will be identical and the interferogram phase will be zero. If there is a current u on the surface, the range will change by $\Delta x \sin \theta = u \cdot (t_2 - t_1) \cdot \sin \theta$ in the time it takes the aircraft to fly the distance between its two antennas. For an aircraft traveling at velocity v , with antennas separated by baseline B , $t_2 - t_1 = B/v$. The observed phase difference will be proportional to the line-of-sight component of the current velocity, and scaled by the sine of the incidence angle:

$$\begin{aligned}
 \Delta\phi &= \frac{4\pi}{\lambda} \Delta x \sin \theta \\
 &= \frac{4\pi}{\lambda} u (t_2 - t_1) \sin \theta \\
 &= \frac{4\pi}{\lambda} \frac{u}{v} B \sin \theta
 \end{aligned}$$

So for a swath-imaging radar interferogram, a map of $\Delta\phi$ gives the surface current distribution toward the radar. Computing the accuracy of a velocity measurement using the same logic we employed for the elevation interferometer, we derive:

$$\sigma_u = \frac{\lambda}{4\pi} \frac{v}{B \sin \theta} \sigma_\phi \quad (17.35)$$

For typical aircraft system parameters,

$$0.1 \text{ m/s} \approx \frac{0.06}{4\pi} \frac{200}{2 \sin 30} 0.1 \text{ rad} \quad (17.36)$$

The velocity uncertainty of about 0.1 m/s is just what is needed for ocean current observations. But if we use a much longer temporal baseline than the short times available on the single aircraft implementation, we can greatly improve the sensitivity to subtler motions. Let us then look at a satellite implementation, where the time between observations can be weeks to years. In this case we will find it more useful to use a phase sensitivity equation of form:

$$\Delta\phi = \frac{4\pi}{\lambda} u_{LOS} (t_2 - t_1) \quad (17.37)$$

where u_{LOS} is the radar line of sight component of velocity. We can also recognize $\Delta r = u_{LOS} (t_2 - t_1)$ as the total line of sight displacement over the time interval $\Delta t = (t_2 - t_1)$, which leads to a slightly different form of the sensitivity equation:

$$\sigma_r = \frac{\lambda}{4\pi} \sigma_\phi \quad (17.38)$$

The deceptively simple equation shows the power of the repeat pass satellite implementation. Let us look at a spaceborne C-band radar satellite interferogram, for which

$$0.005 \text{ m/s} \approx \frac{0.06}{4\pi} 0.1 \text{ rad} \quad (17.39)$$

For a modest phase uncertainty of 0.1 rad, we can measure a displacement of 5 mm. Depending on how long a time span we can use to form an interferogram, we can measure very slow rates indeed. For example, a one year interferogram yields 5 mm/yr sensitivity. This delicate sensitivity to motion permits observations of very detailed motions.

An example deformation image is shown in fig. 17.11. This image depicts the line of sight

displacement coincident with an eruptive event on the island of Hawaii during the first half of 2018. Data were acquired by the Sentinel-1A and -1B spacecraft between 6 MAR 2018 and 28 JUN 2018; the phase difference of each interferogram was scaled by $\frac{\lambda}{4\pi}$ to yield the change in range. Motion is seen mainly along the east rift zone of Kilauea volcano. The rest of the image is fairly stationary, but changes in atmospheric water vapor content lead to apparent motions. For this reason multiple interferograms are averaged for many geophysical investigations, as was done here.

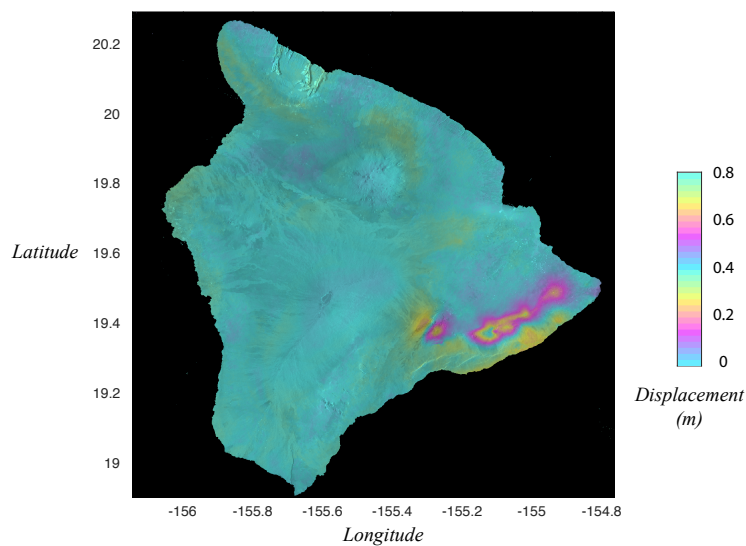


Figure 17.11: Surface deformation at Kilauea volcano in Hawaii. Image presents line of sight displacement coincident with an eruptive event on the island of Hawaii during the first half of 2018. Data were acquired by the Sentinel-1A/1B spacecraft between 6 MAR 2018 and 28 JUN 2018. The phase difference in each interferogram scaled by $\lambda/4\pi$ yields the change in range. Motion is seen mainly along the east rift zone of Kilauea volcano. The rest of the image is fairly stationary, but changes in atmospheric water vapor content lead to apparent motions. For this image, multiple interferograms were averaged to reduce the errors from the variable atmosphere.

17.11 Nonzero baselines

In the two examples previous, we derived elevation and deformation estimates from radar interferograms. We found that separating antenna locations spatially permits us to infer heights, while separating antennas temporally yields sensitivity to motion. It is rather straightforward to create a spatial baseline with zero temporal offset by using a physical array of antennas, but

when we try to implement a temporal baseline it is very challenging to have zero spatial offset. It is generally hard to have a spacecraft, for example, return to exactly to the same spot in space at both acquisition times. So we must ask how this will affect our motion measurements.

We are asking what happens when the across-track component of the baseline is not zero. In that case, we get contributions from both motion and topography. We need to determine the relative sizes of these contributions, and how they can they be separated in order to achieve the greatest accuracy. We begin with an equation for total phase that includes both effects.

$$\phi = -\frac{4\pi}{\lambda}|B|\sin(\theta - \alpha) - \frac{4\pi}{\lambda}\Delta r \quad (17.40)$$

The total phase measured has two components, one from antenna separation in space that depends on surface topography (through $z = r \cos \theta$), and one that depends on any line of sight displacement Δr between observation times. There are two main approaches in common use to isolate each, one denoted the *two-pass method* and one the *three-pass method*. For this discussion, let us assume that we are most interested in surface deformation and that the topographic signal is what we would like to remove from our interferogram.

Two-pass method. The first term on the right hand side of eq. 17.40 is the contribution from the parallax between the two incidence directions. This phase goes to zero if the baseline length is zero, which was the assumption in the derivation we used for a motion interferometer. But it is hard to achieve this in practice, as even what we refer to as repeat orbits do not repeat exactly. Separations from 100's to 1000's of meters are common.

Even if we cannot control satellites to near zero baselines, cross-track orbit knowledge, and thus the InSAR baseline, is often available at the cm level. Further, for many applications, and many parts of the Earth, the topography itself may be known to a few meters or less. In the two-pass method, we use the orbit location and topography information to compute the phase from variations in elevation. We then subtract the modeled phase from the measured total phase and what remains is the contribution from deformation.

We found in eq. 17.25 how σ_z depends on σ_ϕ , which inverted yields

$$\sigma_\phi = \frac{4\pi}{\lambda} \frac{|B| \cos(\theta - \alpha)}{r \sin \theta} \sigma_z \quad (17.41)$$

and thus we can compute how much phase error we might expect from uncertainty in topography or orbital position. Substituting nominal spacecraft C-band repeat pass parameters, we let

$|B|=1000$ m, $\alpha=0$, $\theta = 45^\circ$, $r=800$ km, and $\sigma_z=1$ m, and obtain $\sigma_\phi \approx 0.26$ rad. This corresponds to a line of sight deformation uncertainty of $\lambda/4\pi \cdot 0.26 = 1.3$ mm. In many cases the remaining phase error is small compared to the desired deformation phase.

Three-pass method. We will not always be able to remove the topography-related artifact from our interferograms. This will most often happen when we do not know the topography sufficiently well, or at all, when we analyze an interferogram for crustal deformation. This can be the case for parts of the Earth when topography is either unknown or changeable, and is almost always the case when we are studying other planets. All is not lost, however, as we can use the measurements themselves to derive and remove the topography, as long as we have three satellite passes rather than two.

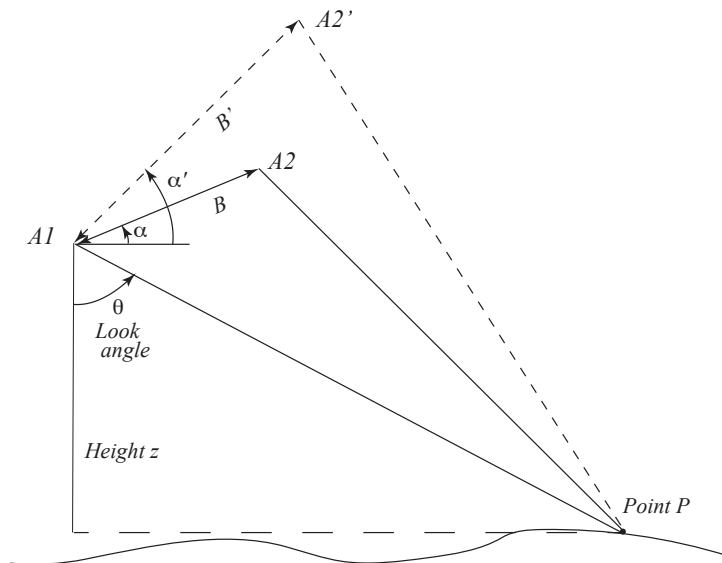


Figure 17.12: Three-pass method. This geometry pertains if we have three passes over our area of interest, rather than two. We form two interferometers, one from $A1$, $A2$, and P (solid lines), and one from $A1$, $A2'$, and P (dashed lines). Comparing the phases from each allows us to remove the topography phase term (see text).

Refer to fig. 17.12. Using the parallel ray approximation to keep things simple, the phase from the unprimed coordinates will be

$$\phi = -\frac{4\pi}{\lambda}|B|\sin(\theta - \alpha) \quad (17.42)$$

and the phase from the primed coordinates is

$$\phi' = -\frac{4\pi}{\lambda}|B'| \sin(\theta - \alpha') \quad (17.43)$$

Note that the two measurements each yield the same estimate of θ , or implied elevation. Our goal is to compute one from the other in order to eliminate the topographic dependence. Their ratio still depends on topography through θ

$$\frac{\phi'}{\phi} = \frac{|B'| \sin(\theta - \alpha')}{|B| \sin(\theta - \alpha)} \quad (17.44)$$

but we can eliminate that dependence by correcting the measured phase for the ‘flat-Earth’ phase, that is the phase that would have been measured in the absence of topography² (fig. 17.13). Defining as ϕ_{flat} the corrected phase after subtracting the flat-Earth phase at look

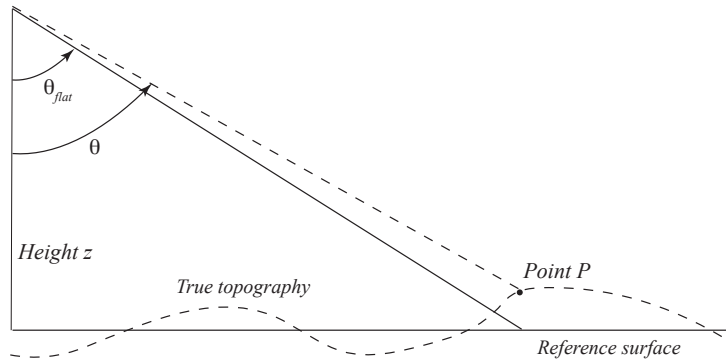


Figure 17.13: Flat Earth phase: the phase pattern that would be observed using an imaging geometry identical to the acquisition under question but assuming that there is no topography present. The look angle for the flat Earth phase is denoted θ_{flat} .

angle θ_{flat}

$$\phi_{flat} = -\frac{4\pi}{\lambda}[|B| \sin(\theta - \alpha) - |B| \sin(\theta_{flat} - \alpha)] \quad (17.45)$$

Since $\theta \approx \theta_{flat}$, we can simplify eq. 17.45 using

$$\theta = \theta_{flat} + \delta\theta \quad (17.46)$$

²Note that if we are using a spherical Earth rather than a truly flat Earth, the reference would be along the curved surface.

$$\begin{aligned}\sin(\theta - \alpha) &= \sin(\theta_{flat} - \alpha + \delta\theta) \\ &\approx \sin(\theta_{flat} - \alpha) + \cos(\theta_{flat} - \alpha)\delta\theta\end{aligned}$$

so that

$$\phi_{flat} = -\frac{4\pi}{\lambda}|B|\cos(\theta_{flat} - \alpha)\delta\theta \quad (17.47)$$

Under these approximations, the flattened phase is now proportional to the perpendicular component of the baseline rather than the parallel component, and to the topographic distortion $\delta\theta$ directly. So now when we form the ratio

$$\frac{\phi'_{flat}}{\phi_{flat}} = \frac{|B'|\cos(\theta_{flat} - \alpha')}{|B|\cos(\theta_{flat} - \alpha)} = \frac{B'_{\perp}}{B_{\perp}} \quad (17.48)$$

it no longer depends on topography. Consider again the total phase equation resulting from both topography and deformation, but this time in terms of flattened phase:

$$\phi_{flat} = -\frac{4\pi}{\lambda}|B|\cos(\theta_{flat} - \alpha) - \frac{4\pi}{\lambda}\Delta r \quad (17.49)$$

Now, further suppose that the time interval corresponding to the primed coordinates is when the point P moves closer to the radar by a distance δr , with no motion in the time covered by the unprimed interferogram. Then we can restate the deformation phase equation using the two flattened phase measurements:

$$\phi'_{flat} - \frac{B'_{\perp}}{B_{\perp}}\phi_{flat} = -\frac{4\pi}{\lambda}\Delta r \quad (17.50)$$

From this we see that we can acquire two interferograms over the same area, and use one to correct for the topographic phase term to yield the deformation phase. This does require knowledge of when deformation occurs, or at least a common rate of displacement, to be able to isolate it from the topography. But it does allow us to be able to form images of displacement when the actual surface shape is unknown.